Zr-Based MOF-545 Metal-Organic Framework Loaded with Highly Dispersed Small Size Ni Nanoparticles for CO2 Methanation

Hongmei Chen, Jean Blaise Brubach, Ngoc Huan Tran, Amanda L. Robinson, Ferdaous Ben Romdhane, Mathieu Frégnaux, Francesc Penas-Hidalgo, Albert Solé-Daura, Pierre Mialane, Marc Fontecave, et al.

Zr-based MOF-545 Metal-Organic Framework Loaded with Highly Dispersed Small Size Ni Nanoparticles for CO_2 Methanation

Hongmei Chen,[a] Jean-Blaise Brubach,[b] Ngoc-Huan Tran,[a] Amanda L. Robinson,[a,c] Ferdaous Ben Romdhane,[d] Mathieu Frégnaux,[c] Francesc Penas-Hidalgo,[a] Albert Solé-Daura,[e] Pierre Mialane,[c] Marc Fontecave,[a] Anne Dolbecq,[c] Caroline Mellot-Draznieks[a,c]**

[a] Laboratoire de Chimie des Processus Biologiques (LCPB), CNRS UMR 8229, Collège de France, PSL University, Sorbonne Université, 75231 Paris, France.
[b] Synchrotron SOLEIL, L'Orme des Merisiers - Départementale 128 - 91190 Saint-Aubin, France.
[c] Institut Lavoisier de Versailles, UVSQ, CNRS UMR 8180, Université Paris-Saclay, 78000, Versailles, France
[d] Fédération de Chimie et Matériaux de Paris-Centre (FCMat), 4 Place Jussieu, 75005, Paris, France

[e] Departament de Química Física i Inorgànica, Universitat Rovira i Virgili, Marcel·lí Domingo 1, Tarragona 43007, Spain

KEYWORDS: Ni-based catalysts, metal-organic frameworks (MOFs), CO_2 hydrogenation, in situ/operando methods, CO_2 methanation

ABSTRACT: We report the use of the Zr-based metal-organic frameworks (MOFs) MOF-545 and MOF-545(Cu) as supports to prepare catalysts with uniformly and highly dispersed Ni nanoparticles (NPs) for CO_2 hydrogenation into CH_4. In the first step, we studied the MOF support under catalytic conditions using operando Diffuse Reflectance Infrared Fourier Transform (DRIFT) spectroscopy, ex-situ characterizations (PXRD, XPS, TEM, EDX-element mapping) and DFT calculations. We showed that the high-temperature conditions undoubtedly confer a potential for catalytic functionality to the solid towards CH_4 production, while no role of the Cu could be evidenced. The MOF was shown to be transformed into a catalytically active material, amorphized but still structured with dehydroxylated Zr_6-oxoclusters, in line with DFT calculations. In the first step, Ni@MOF-545 catalysts were prepared using either the impregnation (IM) or double solvent (DS) methods, followed by a dry reduction route under H_2 to immobilize Ni NPs. The highest catalytic activity was obtained with the **Ni@MOF-545 DS** catalyst (595 $mmol_{CH4}$ g_{Ni}^{-1} h^{-1}) with 100% CH_4 selectivity and 60% CO_2 conversion after ~3h. The much higher catalytic activity of **Ni@MOF-545 DS** is a result of much smaller (~ 5 nm) and better dispersed Ni NPs than in the IM sample (20-40 nm), the latter exhibiting sintering. The advantages of the encapsulation of Ni NPs by the DS method and of the use of MOF-545-based support are

discussed, highlighting the interest of designing yet-unexplored Zr-based MOFs loaded with Ni NPs for CO_2 hydrogenation.

INTRODUCTION

The conversion of CO_2 into commercially valuable chemicals (such as methane,[1,2] formic acid,[3,4] methanol,[5] and ethanol[6–8]) is a promising strategy as a way to move towards a low-carbon chemical industry. The CO_2 methanation reaction ($CO_2 + 4H_2 \rightarrow CH_4 + 2H_2O$, ΔH_{298K} = -164 kJ/mol), also named the Sabatier reaction, was first reported in 1902.[9] The conversion of CO_2 to methane consumes hydrogen gas, which can be produced by solar-driven water splitting or water electrolysis using renewable electricity.[10] Interestingly, CO_2 methanation is an attractive option for renewable hydrogen storage as methane has a higher chemical energy density than hydrogen, and also because our society has all the infrastructure needed to transport, store and burn methane. Pd, Ru, Rh and Ni-based catalysts were reported for CO_2 methanation over the past decades.[11] Among them, systems incorporating nickel have been extensively studied as being low price and noble metal-free catalysts while delivering high performances with excellent CH_4 selectivity.[12–14]

Metal-organic frameworks (MOFs) are porous solids which can provide abundant active sites for catalytic reactions. In the last decade, there has been a surge of interest in MOFs within the realms of CO_2 adsorption, gas separation and catalysis owing to their remarkable attributes such as a large surface area, tunable porosity, strong metal binding sites and the capacity for tailored metal-support interactions.[15] In the realm of CO_2 hydrogenation, MOFs have emerged as pivotal supports or sacrificial precursors, playing a promising role in the fabrication of efficient catalysts.[16–18] MOF-based catalysts may be specifically designed to ensure the uniform dispersion of metal nanoparticles (NPs) and augment the interplay between NPs and the support, effectively preventing the undesired phenomena of sintering and aggregation of active metal species.[19,20] In particular, a number of Ni-containing MOF catalysts have been reported in the last decade for CO_2 methanation, exploiting the high dispersion of small size Ni NPs, including Ni@MOF-5,[21] Ni@MIL-101-Cr,[22,23] and Ni@UiO-66.[22,24] Moreover, MOF-derived Ni-containing systems have been also reported as sacrificial precursors for the synthesis of efficient catalytic materials, via high temperature (> 500 °C) pyrolysis.[25–27] Overall, these studies shed light on key features that determine the performances of these Ni-based catalysts, such as the impact of the metal immobilization methods, the nickel reduction conditions or the Ni loading, in addition to the catalytic conditions themselves (temperature, reactants ratio…). In parallel, the catalytic activities also known to be strongly dependent on the support used (SiO_2, CeO_2, TiO_2, ZrO_2 or MgO).[28] Importantly, zirconia is a support known to promote CO_2 hydrogenation, allowing strong Ni-ZrO_2 interfacial sites.[29] Along this line, the Zr-based MOF UiO-66 was recently used as a precursor to produce a porous hydrous zirconia support for a highly dispersed Ni catalyst, resulting in an efficient and stable catalyst for CO_2 methanation.[30] So far, UiO-66 is the only Zr-based MOF used as a support for dispersing metallic Ni NPs for CO_2 methanation, leaving other Zr-based MOF unexplored. Still, Zr-based MOFs form a potentially interesting sub-family of solids whereby their porosity may be used to disperse Ni NPs while their Zr_6-oxoclusters may mimic the ZrO_2-type support.

Herein, we report the immobilization of nickel NPs in the Zr-based MOF-545 and MOF-545(Cu) (**Figure 1**) and their use as Ni-based heterogeneous Ni@MOF catalysts for the hydrogenation of CO_2. Our choice of MOF-545 as a support was driven by the specific features of this hybrid framework, which combines: i) built-in Zr_6-oxocluster nodes, ii) very large pores system for immobilizing Ni NPs and iii) porphyrin organic linkers amenable to additional metalation. We targeted the Cu-metalated MOF-545 because Cu-containing MOFs recently attracted attention for their CO_2 hydrogenation

activities.[31–33] MOF-545 crystal structure exhibits hexagonal and triangular 1D channels aligned parallel to the *c*-axis with diameters of 36 Å and 9 Å, respectively (**Figure 1a**, left), being based on Zr_6O_8 oxocluster nodes connected to each other via 8 porphyrin linkers.

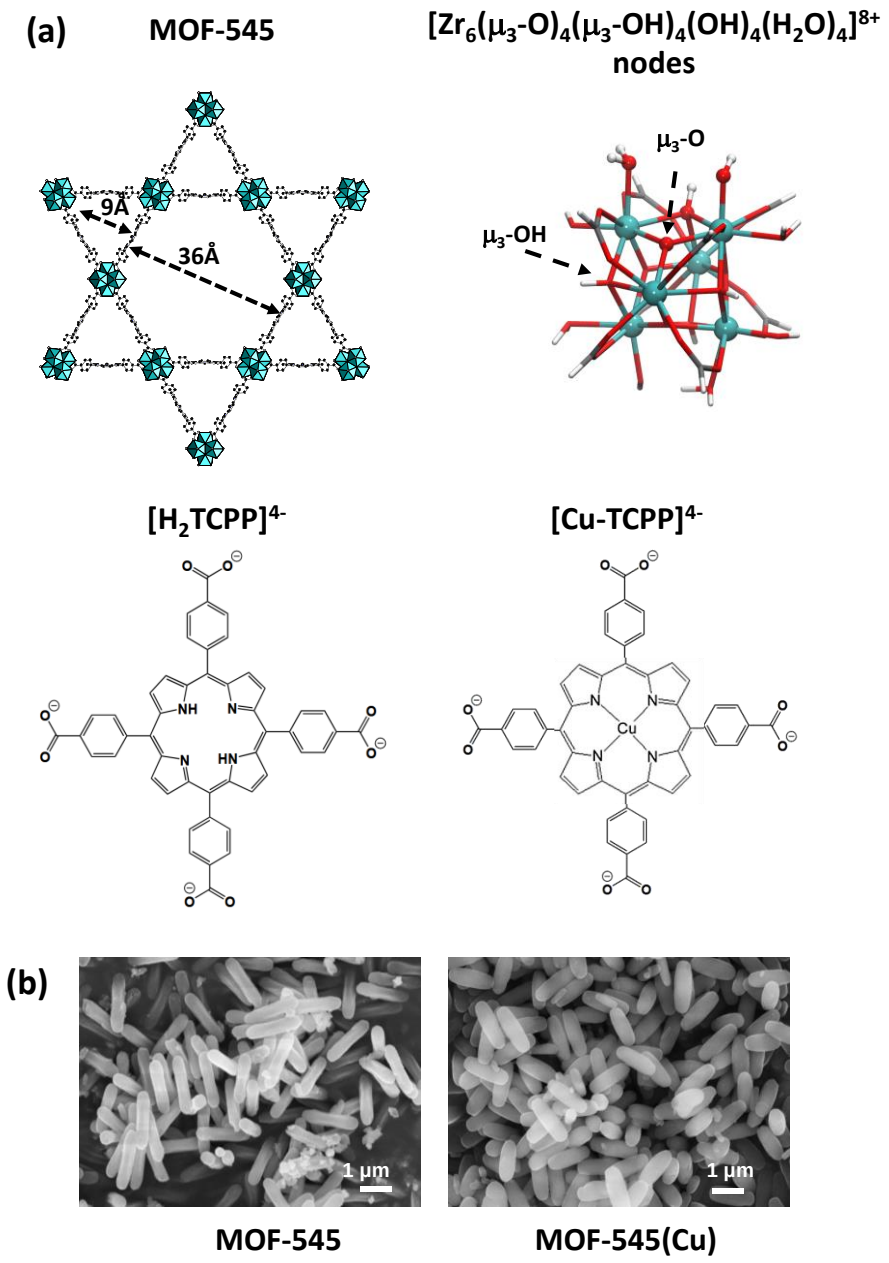

Figure 1. (a) Porous structure of **MOF-545** and **MOF-545(Cu)** showing the individual Zr-oxocluster (ZrO_8: blue octahedra, Zr: blue spheres, O: red spheres, H: grey spheres) and the porphyrin linkers. (b) SEM images of **MOF-545** and **MOF-545(Cu)** as-synthesized in this work.

In each Zr-node, the six Zr^{4+} metal atoms form an octahedron with 4 μ_3-OH or 4 μ_3-O moieties coordinated at each face of the octahedron (**Figure 1a**, right). In the present work, both parent materials MOF-545 and MOF-545(Cu) were first studied for CO_2 hydrogenation, with the aim to explore their behaviour (i.e. in the absence of Ni NPs) under catalytic conditions. In a second step, the catalytic performances of the derived Ni@MOFs solids were then explored. Particular attention was given to the method used to disperse the Ni^{2+} precursor cations within the channels of MOF-545 and MOF-545(Cu). Two methods were employed, the traditional impregnation method (IM) and the

double solvent method (DS), both followed by a dry route reduction of Ni^{2+} under H_2 flow. This approach allowed comparing the catalytic activities of the various solids obtained upon the preparation (IM/DS) method alone and then upon the H_2 reduction treatment.

RESULTS AND DISCUSSION

Investigation of MOF-545-derived supports.

Preparation and characterization of Zr-based MOFs supports. Rod-like shape crystals of the Zr-based MOF-545 and MOF-545(Cu) (**Figure 1b**) were synthesized following reported synthetic procedures[34] and characterized by powder X-ray diffraction (PXRD) and thermogravimetric analysis (TGA) (**Figures S1 and S2**, respectively). The as-synthesized MOF-545 and MOF-545(Cu) solids were further studied by DRIFT spectroscopy (**Figure 2a-b**), confirming the expected chemical differences between MOF-545 and MOF-545(Cu). The non-metalated porphyrins in MOF-545 indeed exhibited the characteristic stretching and bending vibrations of the N-H of TCPP at 967 cm^{-1} and 3321 cm^{-1}.[31] In contrast, these vibrations were absent in the FT-IR spectrum of MOF-545(Cu), while a strong characteristic symmetric stretching vibration of $C\text{-}N_{Cu}$ coordination bonds was observed at around 1006 cm^{-1},[31] supporting the successful metalation of the porphyrin linkers. Both solids show intense ν(OH) stretching of μ_3-OH groups with characteristic signals at 3671 cm^{-1} [35] together with the $Zr\text{-}\mu_3O$ peaks at 655-750 cm^{-1}.[36] This is in line with MOF-545 and MOF-545(Cu) possessing the same constitutive Zr_6-oxocluster nodes.

In situ DRIFT studies of the MOF-545 and MOF-545(Cu) supports under catalytic conditions. We then investigated the catalytic CO_2 hydrogenation activities of the as-synthesized solids MOF-545 and MOF-545(Cu) in order to identify possible modifications of their structures under catalytic conditions (CO_2/H_2 flow rate at 3/9 mL min^{-1} at 10 bar up to 300°C). The flow reactor was equipped with an in-situ DRIFT setup and a gas chromatograph (GC) (**Figure S3a**) for detection of products. Both MOF-545 and MOF-545(Cu) exhibited very similar behaviours in terms of catalytic activities towards methane production, excluding a role for Cu during catalysis (**Figure S4**). Hence, only the results obtained for MOF-545(Cu) are discussed in detail below. The impact of temperature on CO_2 hydrogenation was studied by increasing the flow reactor temperature step by step, from RT up to 300 ˚C (RT, 120˚C, 200˚C, 300˚C) at 10 bar under CO_2/H_2 (1:3) flow. The *in-situ* DRIFT responses of **MOF-545(Cu)** under such CO_2 hydrogenation conditions upon increasing temperature and time are shown in **Figure 2c-d** and **Figure S5**.

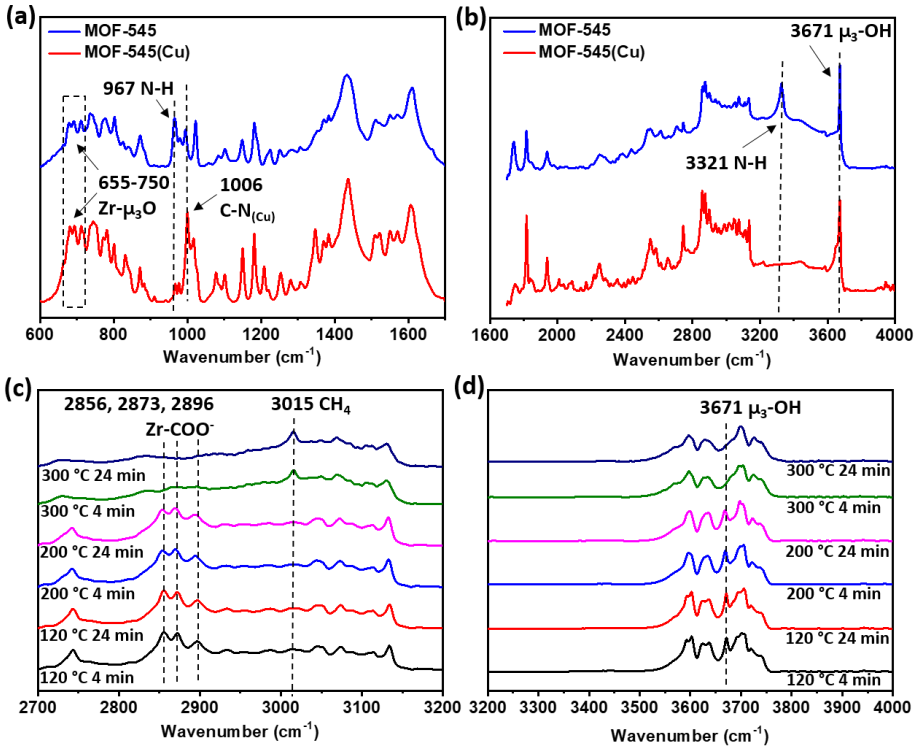

Figure 2. (a) and (b) DRIFT absorption spectra of the as-synthesized **MOF-545** and **MOF-545(Cu)** MOFs. (c) and (d) In situ DRIFT absorption spectra of **MOF-545(Cu)** under CO_2 hydrogenation conditions at different temperatures in flow reactor conditions (15 mg of catalyst, CO_2/H_2 flow rate at 3/9 mL min^{-1}, flow reactor pressure at 10 bar).

CH_4 was detected via its characteristic symmetric stretching at 3015 cm^{-1} as the major product when the temperature was increased up to 300˚C (**Figure 2c**) and quantified by GC (**Figure S4**). Traces of CO could be detected by high-resolution DRIFT (**Figure S6**). Also, no CH_4 product was detected at lower temperatures, i.e. 120˚C and 200˚C. Notable modifications of the MOF's IR spectra were also observed at 300˚C in the regions of the bridging μ_3-OH groups and the ν(C-H) stretching modes of TCPP phenyl groups. The peak of the bridging μ_3-OH groups at 3671 cm^{-1}, typical of ν(OH) stretching in Zr-based MOFs,[37–39] was absent from the IR spectra at 300˚C (**Figure 2d**), revealing the dehydroxylation of the MOF. Also, the IR group of peaks associated with the $\nu(C\text{-}H)_{phenyl}$ stretching modes (2856 cm^{-1}, 2873 cm^{-1}, and 2896 cm^{-1})[40] were erased at 300˚C (**Figure 2c**). We hypothesized that these vibrations were affected by modifications of the neighbouring Zr_6-oxoclusters. In contrast, the symmetric stretching of the $C\text{-}N_{Cu}$ bond was only slightly shifted over the whole range of temperature (1006 cm^{-1}),[31] showing that Cu remained coordinated to the porphyrinic linkers. The dehydroxylation and the modified $\nu(C\text{-}H)_{phenyl}$ stretching modes are maintained over the continuous CH_4 production event, as illustrated by the time-evolution of this IR region (**Figure S7**).

In order to identify the carbon's origin of CH_4, catalytic tests were performed with labelled $^{13}CO_2/H_2$ gas mixture recording DRIFT spectra every 4 min over 1h. Only $^{13}CH_4$ was detected, as the IR spectra exhibited the characteristic peak of $^{13}CH_4$ at 3005 cm^{-1}, instead of 3015 cm^{-1} typical of $^{12}CH_4$ (**Figure S8a**). A continuous production of $^{13}CH_4$ over time was observed together with no detection of $^{12}CH_4$ (**Figure S8b**). This provided evidence that CH_4 was indeed produced from the CO_2 flow, with no methane emanating from the MOF's decomposition.

The above results point towards significant modifications of the MOF in the 200°C-300°C range, temperatures at which the MOF is still structured and the complete linker's decomposition has not

occurred yet, as indicated by the TGA curve (**Figure S2**) and the maintained features of the porphyrin in the 1400-1650 cm^{-1} region (**Figure S5b**). They show that the conversion of CO_2 into methane may proceed at 300°C, after substantial structural modifications to the Zr-based MOF-545 have occurred with the dehydroxylation of the Zr_6-oxoclusters. The catalytic activity of MOF-545 is subsequent to these structural transformations upon thermal treatment, which motivated us to further undertake a computational study on the behaviour of the Zr_6-oxoclusters upon thermal treatment, as detailed below.

DFT calculations on Zr_6-oxoclusters. Beyond the loss of Zr-coordinated water molecules upon dehydration, dehydroxylation is known to occur in Zr-based MOFs upon heating and mechanistic pathways have been elucidated for the Zr_6-oxocluster nodes in the well-known UiO-66 hybrid framework.[41,42] Typically, an -OH group abstracts a proton from a vicinal μ_3-OH group, leaving a water molecule and a μ_3-O behind as well as an under-coordinated Zr^{4+} metal site. Using Pair Distribution Function analysis and DFT calculations, further restructuring upon heating up to 350˚C was also evidenced in the large pore NU-1000 MOF - the latter sharing similar architecture and Zr-based nodes as MOF-545 but incorporating tetratopic 1,3,6,8-tretrakis(*p*-benzoate)pyrene linkers instead of TCPP ones.[43] The reported restructuring consisted of local and disordered distortions of the Zr-nodes, identified as distinct of the well-known dehydration/dehydroxylation events. In order to gain a greater understanding of the transformations of the Zr_6-oxoclusters in MOF-545, DFT calculations (see details in SI) were performed on its fully coordinated $[Zr_6O_8(OH)_4(H_2O)_4]$ nodes (**Figure S9a**) and explored its dehydration and dehydroxylation processes. The DFT calculations show that the exergonic dehydration process may occur at mild temperatures through the loss of the water molecules coordinated to the Zr^{4+} sites (**Scheme S1**). The resulting dehydrated cluster, $[Zr_6O_8(OH)_4]$, may undergo successive dehydroxylations, the whole process being exergonic at high temperatures. The relatively low-energy transition state identified for the first dehydroxylation step (13.1 kcal mol^{-1}) indicates a kinetically feasible step. The dehydroxylated cluster exhibits a distorted structure whereby an octahedral environment around Zr^{4+} sites is created through rearrangement of the linker's carboxylates and oxo groups (**Figure S9b**). Also, additional exploratory calculations suggested that the dehydroxylated cluster may be able to activate CO_2 and H_2 under CO_2/H_2 pressure (**Scheme S1**), which could be related to the early steps of the experimentally observed CO_2 hydrogenation. In fact, relying on DFT calculations, Yang et al. proposed a reaction pathway for CO_2 hydrogenation into methanol catalysed by similar Zr_6-oxoclusters in UiO-66.[44] Nevertheless, further experimental and computational work is certainly required to elucidate the mechanism underlying CO_2 methanation at play here.

Post-catalytic characterizations. To further probe the possible modifications of the MOF upon catalysis, *ex-situ* characterizations (PXRD, XPS, TEM and EDX-element mapping) were performed after CO_2 hydrogenation at 300 ˚C for the **MOF-545(Cu)** sample. While the XRD pattern shows a significant loss of crystallinity after catalysis (**Figure S10**), XPS of MOF-545(Cu) after catalysis shows that all Cu were maintained in their 2+ oxidation state and Zr centres in Zr^{4+} state, as in the as-synthesized MOF (**Figure S11a-b**). EDX elemental mapping reveals a similar dispersion of Cu in the rods of MOF-545(Cu) before and after catalysis (**Figure S12a-b**). Finally, TEM images show that the rod morphology of the MOF crystals was preserved upon catalysis leading to slightly shrunk rods (**Figure S12b**). Overall, the post-catalytic characterizations together with the above *in-situ* DRIFT observations allow us to draw a portrait of the transformed MOF as being a catalytically active material for CO_2 hydrogenation. Under the catalytic conditions used here, this material - which will be used as further support for Ni NPs (see next section) - is significantly amorphized although still structured with reconstructed Zr_6-oxoclusters.

Investigation of Ni@MOF catalysts for CO_2 methanation

Impact of the preparation method on catalytic activities. We further prepared Ni@MOF catalysts by introducing Ni NPs in MOF-545 and MOF-545(Cu) and tested their catalytic performances for CO_2 methanation. These materials were prepared in two steps. We first used the traditional impregnation method (IM) for preparing **Ni@MOF-545 IM** and **Ni@MOF-545(Cu) IM** using the as-synthesized MOF-545 and MOF-545(Cu) and $Ni(NO_3)_2$•$6H_2O$ as Ni precursor source. Notably, the IM method lead to a partial amorphisation of the MOF supports (**Figure S13**). In order to form metallic Ni^0 NPs, a dry reduction route was further adopted under a 5 vol.% H_2/Ar flow at 350 °C for 24 h in a tube furnace. PXRD patterns confirmed the successful reduction of Ni^{2+} into Ni^0 as the resulting **Ni@MOF-545 IM R** and **Ni@MOF-545(Cu) IM R** (R = reduced) solids exhibited intense diffraction peaks at 44.7°(*2θ*) and 52.0°(*2θ*), which are characteristic of metallic Ni^0 planes (111) and (200), respectively (**Figure S14**). We noted, however, that the H_2 reduction treatment led to the full amorphisation of the MOF supports. ICP-MS analysis indicated that the Ni loading reached 37.6 wt % and 35.9 wt % in **Ni@MOF-545 IM R** and **Ni@MOF-545(Cu) IM R**, respectively (**Table S1**).

The catalytic activities of reduced solids were then evaluated over 3 h screening tests in static conditions (CO_2/H_2 in 1:3 ratio, 10 bar, 300˚C, **Figure S3b**) and products quantified by GC. For reference purposes, we first prepared and tested **MOF-545 R** and **MOF-545(Cu) R**. Expectedly, both solids exhibited rather low catalytic activities, producing CH_4 and CO in the 15-41 μmol g_{cat}^{-1} h^{-1} range and up to 12 μmol g_{cat}^{-1} h^{-1}, respectively (**Figure 3a**, **Table 1**). We then investigated the two related solids loaded with Ni^0 NPs, **Ni@MOF-545 IM R** and **Ni@MOF-545 IM(Cu) R**. Their CH_4 production rates were boosted in the 4200-4500 μmol g_{cat}^{-1} h^{-1} range, higher by two orders of magnitude than those obtained with their Ni-free counterparts (**Figure 3a**, **Table 1**). Also, the beneficial impact of the H_2 reduction treatment on the catalytic activities is apparent when comparing the performances of the reduced Ni-loaded catalysts to those of their non-reduced counterparts, i.e. **Ni@MOF-545 IM** and **Ni@MOF-545(Cu) IM**. The reduction treatment boosted the CH_4 production rates by a factor of 48 and 36, respectively, while allowing a 100% selectivity towards CH_4 (**Table 1**). Still, we noted that both reduced Ni-loaded materials reached similar catalytic activities after 3 h regardless of the Cu loading. We thus concluded that Cu had no impact on CH_4 production and continued our investigation without using Cu.

As a further attempt to increase the catalytic performances, we modified the Ni loading procedure by using the double solvent method (DS),[45] known to facilitate the deposition of NPs within the pores of MOFs.[45,23,22] MOF-545 was used to prepare **Ni@MOF-545 DS**. The pristine MOF-545 was first introduced in a non-polar solvent (pentane). In the present case, MOF-545 exhibits a built-in spatial partitioning of hydrophobic regions (porphyrinic linkers) and hydrophilic ones (hydroxylated and hydrated Zr_6-oxoclusters). A small amount of aqueous solution of the Ni^{2+} precursor was then introduced slowly, so that the Ni species could diffuse within the MOF's pores towards its hydrophilic parts. Since the inner surface area of MOF-545 is much larger than its outer surface area, the small amount of aqueous solution is prone to diffuse into the MOF's pores by capillary forces, minimizing the deposition on the outer surface in contrast with the conventional single-solvent impregnation method. PXRD and BET measurements of the **Ni@MOF-545 DS** solid showed it was amorphous and non-porous, indicating that the Ni loading step was responsible for both the losses of crystallinity and porosity. After the Ni-loading step, a similar H_2 reduction was applied as previously described allowing the formation of metallic Ni^0 as evidenced by its PXRD pattern (**Figure S15**), resulting in the **Ni@MOF-545-DS R** solid. It was apparent that the resulting material **Ni@MOF-545 DS R** was amorphous, although showing IR vibrations typical of the porphyrin linkers (**Figure S16a**). The integrity of the porphyrins was further confirmed through an in-depth analysis of C 1s XPS spectral lines (vide infra).

A Ni loading of 23.0 wt % in **Ni@MOF-545 DS R** was measured by ICP-MS (**Table S1**), which is significantly lower than the one reached using the IM method (37.6%). Testing its catalytic activity for CO_2 methanation under static conditions, **Ni@MOF-545 DS R** reached a methane production rate of 16866 $\mu mol_{CH4}\ g_{cat}^{-1}\ h^{-1}$, which is 4 times higher than that of its **Ni@MOF-545 IM R** counterpart (4209 $\mu mol_{CH4}\ g_{cat}^{-1}\ h^{-1}$) (**Figure 3a, Table 1**). Normalizing the catalytic activity per Ni, the CH_4 production rate of **Ni@MOF-545 DS R** (73330 $\mu mol_{CH4}\ g_{Ni}^{-1}\ h^{-1}$) is more than 6 times higher than that of **Ni@MOF-545 IM R** (11691 $\mu mol_{CH4}\ g_{Ni}^{-1}\ h^{-1}$).

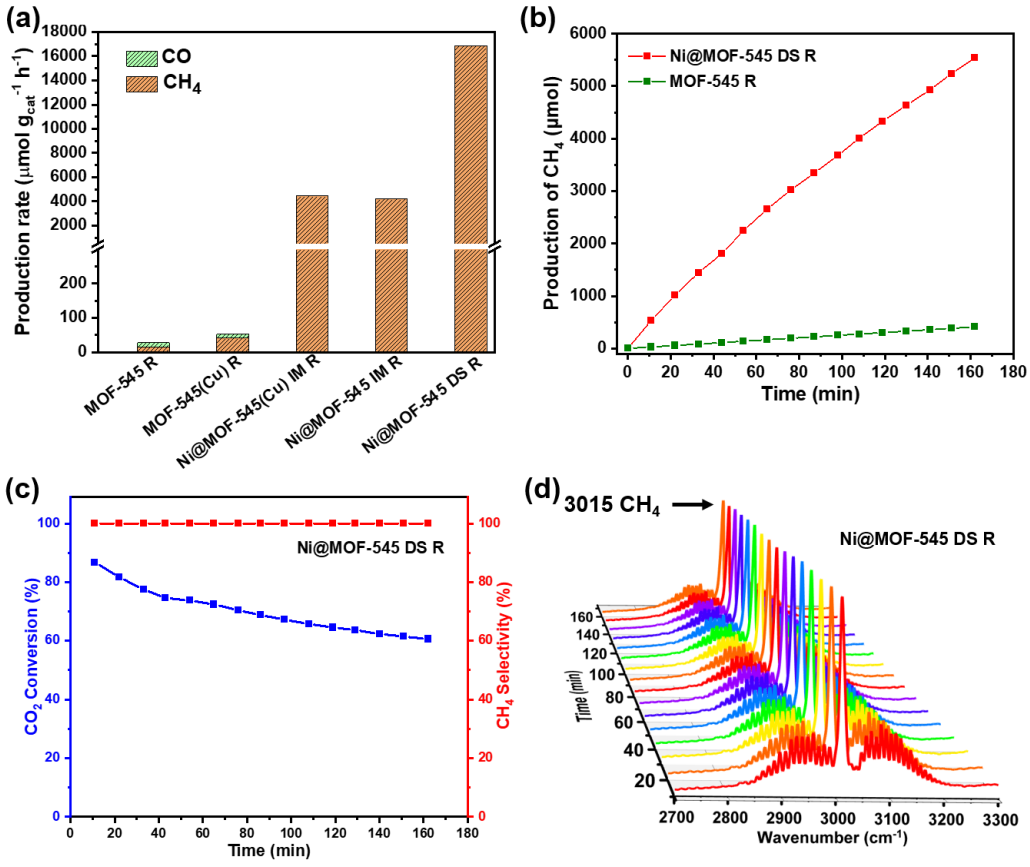

Figure 3. (a) The CH_4 production rates obtained with the reduced MOF-based catalysts reported in this work using static conditions (CO_2/H_2 ratio 1:3, 10 bar, 300˚C, 3h). Rates are averaged over the 3h. (b) Time evolution of CH_4 production using **Ni@MOF-545 DS R** and **MOF-545 R** catalysts for CO_2 methanation in flow reactor conditions (15 mg of catalyst, $CO_2/H_2/N_2$ flow rate of 3/9/10 mL min^{-1}, 10 bar, 300 ˚C, 162 min). (c) CO_2 conversion (%) and CH_4 selectivity of CO_2 methanation over time obtained with **Ni@MOF-545 DS R** in flow reactor conditions. (d) Time-evolution of the *in-situ* DRIFT spectra with a 10 min step during CO_2 methanation experiment using **Ni@MOF-545 DS R** in flow reactor conditions.

Table 1. Comparison of the catalytic performances of MOF-based catalysts for CO_2 methanation in static conditions.

Catalyst	T. (°C)	P (bar)	Select.$_{CH4}$ (%)	Select.$_{CO}$ (%)	Rate$_{CH4}$ ($\mu mol \cdot g_{cat}^{-1} \cdot h^{-1}$) [a]	Rate$_{CO}$ ($\mu mol \cdot g_{cat}^{-1} \cdot h^{-1}$) [a]
MOF-545 R	300	10	56	44	15	12
MOF-545(Cu) R	300	10	77	23	41	12
Ni@MOF-545 IM R	300	10	100	0	4209	0
Ni@MOF-545 IM	300	10	94	6	88	6
Ni@MOF-545(Cu) IM R	300	10	~100	~0	4447	7
Ni@MOF-545(Cu) IM	300	10	54	46	124	104
Ni@MOF-545 DS R	300	10	100	0	16866	0
Ni@MOF-545 DS	300	10	8	93	115	1392

[a] CO_2 methanation in static conditions: 15 mg of catalyst, CO_2/H_2 ratio 1: 3, 10 bar, 300°C, 3h.

Considering the above catalytic activity reached by **Ni@MOF-545 DS R -** the highest of all measured in static conditions - we further investigated its catalytic performances for CO_2 methanation under flow conditions ($CO_2/H_2/N_2$ flow rate 3/9/10 mL min^{-1}, 10 bar, 300 °C) using in situ DRIFT coupled with online GC analysis. The time evolution of CH_4 production by **Ni@MOF-545 DS R** is shown in **Figure 3b** and compared to that of the reference **MOF-545 R**. CH_4 production exhibits a quasi-linear increase with time with 5543 µmol of CH_4 produced at 162 min, allowing to estimate a production rate of 136 864 $\mu mol_{CH4}\ g_{cat}^{-1}\ h^{-1}$ (594 545 $\mu mol_{CH4}\ g_{Ni}^{-1}\ h^{-1}$). Besides its 100% CH_4 selectivity, **Ni@MOF-545 DS R** exhibited better catalytic performances for CO_2 methanation than any Ni@MOF based catalysts reported so far (**Table S2**). In flow reactor conditions, the CO_2 conversion slightly decreased over time (see calculation method in Experimental Section) reaching 60% after 162 min **(Figure 3c**). This deactivation may result from the reoxidation of the Ni metallic sites by the large amount of water produced over the methanation reaction inside the reactor, thus directly damaging the catalytic activity. We found that a reactivation of the **Ni@MOF-545 DS R** solid under successive H_2:Ar treatments at 350°C allowed to recover its full catalytic activity (**Figure S17**). Of note, the methane production rate in static conditions of **Ni@MOF-545 DS R** was only 16866 $\mu mol_{CH4}\ g_{cat}^{-1}\ h^{-1}$ (73330 $\mu mol_{CH4}\ g_{Ni}^{-1}\ h^{-1}$) (**Table 1**) which is expectedly much lower than that in the flow reactor due to the pressure limitations in static conditions. Consistently, the *in-situ* DRIFT spectra recorded every 10 min during the CO_2 methanation experiment exhibited a continuous production of CH_4 (**Figure 3d**).

XPS, TEM and DRIFT characterizations of Ni@MOF materials.

We thought that uncovering the structural and chemical differences between **Ni@MOF-545 IM R** and **Ni@MOF-545 DS R** was essential in order to understand the much better performances of the catalyst prepared with the DS method. The chemical states of Ni in both samples were analysed by X-ray photoelectron spectroscopy (XPS). **Figure 4a** shows Ni 2p XPS spectra of **Ni@MOF-545 IM R** and **Ni@MOF-545 DS R** catalysts. It should be noted that for nickel compounds the spin-orbit splitting of the $2p_{3/2}$ and $2p_{1/2}$ is large enough, so that only the more intense $2p_{3/2}$ signal can be considered. In our case, the Ni $2p_{3/2}$ spectral line is composed of three contributions: (i) a sharp peak centred at 852.2 eV associated with Ni^0, (ii) a broader component at 855 eV attributed to Ni^{2+} species and (iii) satellites peaks (shake-up, plasmons) at around 860 eV.[46–48] The Ni 2p spectral region of **Ni@MOF-545 IM R**

is dominated by the metallic Ni^0 contribution and the corresponding plasmons, while that of **Ni@MOF-545 DS R** mainly exhibits the typical Ni^{2+} signature and a small shoulder at lower binding energy due to the presence of metallic nickel. Still, Ni^0 is detected at the surface of both compounds. The greater proportion of Ni^{2+} detected in the case of **Ni@MOF-545 DS R** can be explained by a more pronounced superficial oxidation of the metal site prior XPS analysis, due to significantly smaller size NPs (vide infra). The Zr 3d core level spectra of the two **Ni@MOF-545 IM R** and **Ni@MOF-545 DS R** catalysts were also investigated by photoemission spectroscopy (**Figure 4b** and **4d,** respectively). In both cases, a doublet with well resolved spin-orbit splitting (2.4 eV) is observed with Zr $3d_{5/2}$ peak positions measured at 181.8 (IM) and 181.4 (DS) eV, respectively. In addition, **Figures 4c-d** compare the XPS spectral lines of Zr 3d respectively in **Ni@MOF-545 DS** and **Ni@MOF-545 DS R**, i.e. before and after reduction. Typical signal similar to stoichiometric ZrO_2 (expected at 182.7 eV)[49] is observed before reduction. The reduced **Ni@MOF-545 DS R** solid shows a large shift to lower binding energies, down to 181.4 eV for the Zr $3d_{5/2}$, which is interpreted as emanating from the potential presence of oxygen vacancies in the reduced sample, in line with previous reports.[48-52] Interestingly, the larger shift in the DS catalyst than in the IM solid would indicate a larger amount of such vacancies. Regarding the C 1s spectral lines (**Fig. 4e-f**), the XPS shows that the aromatic chemical environment of carbon atoms at 284.1 eV characteristic of the porphyrins is maintained upon reduction of **Ni@MOF-545-DS**, together with that of the carboxylates at 288.2 eV, supporting our observations from DRIFT (**Figure S16**) suggesting the integrity of porphyrinic linkers.

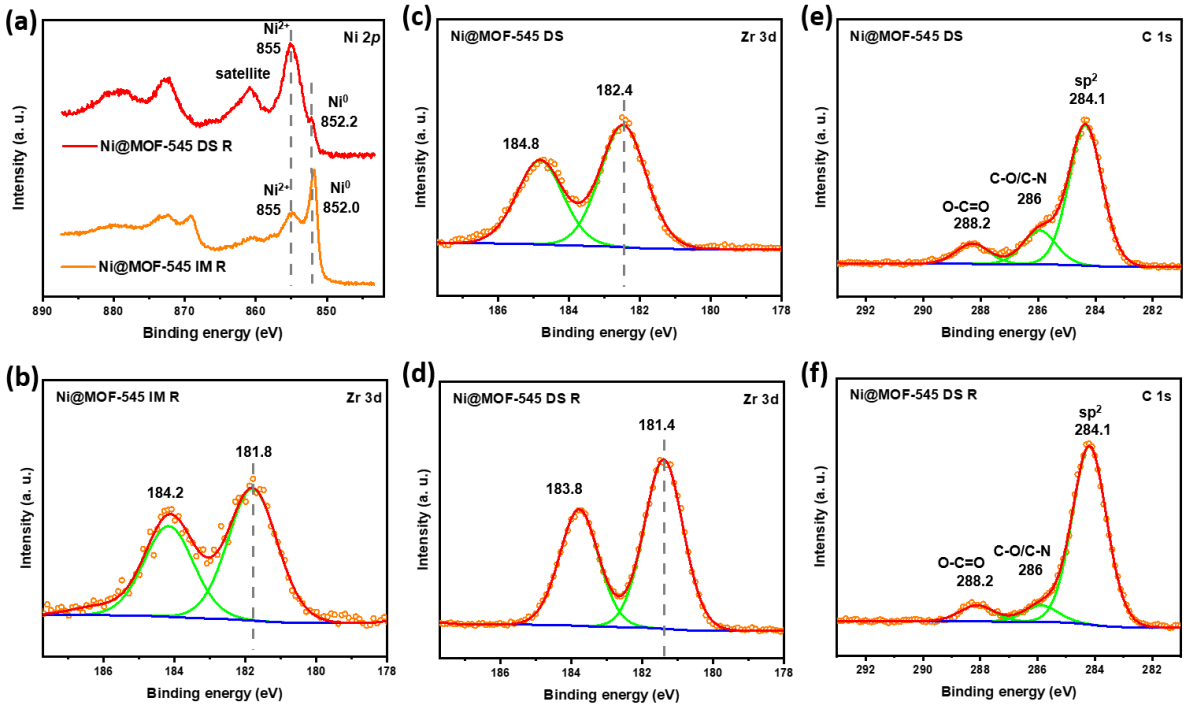

Figure 4. XPS spectral lines of (a) Ni 2p of **Ni@MOF-545 IM R** and **Ni@MOF-545 DS R**, Zr 3d core level of (b) **Ni@MOF-545 IM R** , (c) **Ni@MOF-545 DS** (before reduction) and (d) **Ni@MOF-545 DS R** (after reduction), C 1s of (e) **Ni@MOF-545 DS** (before reduction) and (f) **Ni@MOF-545 DS R** (after reduction).

The morphology and distribution of Ni NPs in **Ni@MOF-545 IM R** and **Ni@MOF-545 DS R** were characterized by TEM, HAADF-STEM and EDX-element mapping. The TEM images of **Ni@MOF-545 IM R (Figure S18a)** clearly showed that Ni^0 NPs have large sizes in the 30-40 nm range and are distributed exclusively over the surface of the MOF's rods, in line with the intense Ni^0 peaks observed in the PXRD pattern (**Figure S14**). In contrast, the TEM images of **Ni@MOF-545 DS R** catalyst

exhibited much smaller Ni NPs around 5 nm size (**Figure S18b**), which are highly dispersed and homogeneously distributed both at the surface of the MOF support and within the bulk of the solid. The small size of these Ni^0 NPs in **Ni@MOF-545 DS R** is also consistent with its PXRD pattern, showing very broad peaks at 44.7° and 52.0 (*2θ*) (**Figure S15**). The EDX-elemental mappings of both IM- and DS-prepared samples confirmed their distinct spatial distribution of Ni^0 NPs (**Figure S18a-b**).

We also performed post-catalytic characterizations of **Ni@MOF-545 DS R** and **Ni@MOF-545 IM R** by TEM, HAADF-STEM, and EDX-element mapping, shown in **Figure 5a-e**. For both **Ni@MOF-545 IM R** and **Ni@MOF-545 DS R**, the morphology and the distribution of Ni NPs are similar before and after the catalytic events. For **Ni@MOF-545 IM R**, the size distribution of Ni NPs indeed remains in the 20-40 nm range after catalysis (**Figure 5a**). For **Ni@MOF-545 DS R,** the Ni NPs are still highly dispersed after catalysis (**Figure 5b**), with a small increase in the Ni NPs' size up to ~6 nm. Further HR-TEM image of the post-catalysis **Ni@MOF-545 DS R** sample (**Figure 5c**) revealed the crystal structure of loaded Ni NPs exposing Ni^0 (111) planes (d = 0.2 nm), which is confirmed by their fast-Fourier-transformed (FFT) image (**Figure 5c** insert). The PXRD pattern of **Ni@MOF-545 DS R** after catalysis showed the same broad Ni^0 (111) peak than the pristine catalyst (**Figure S15**), further supporting that the metallic Ni NPs are maintained after catalysis with no sintering.

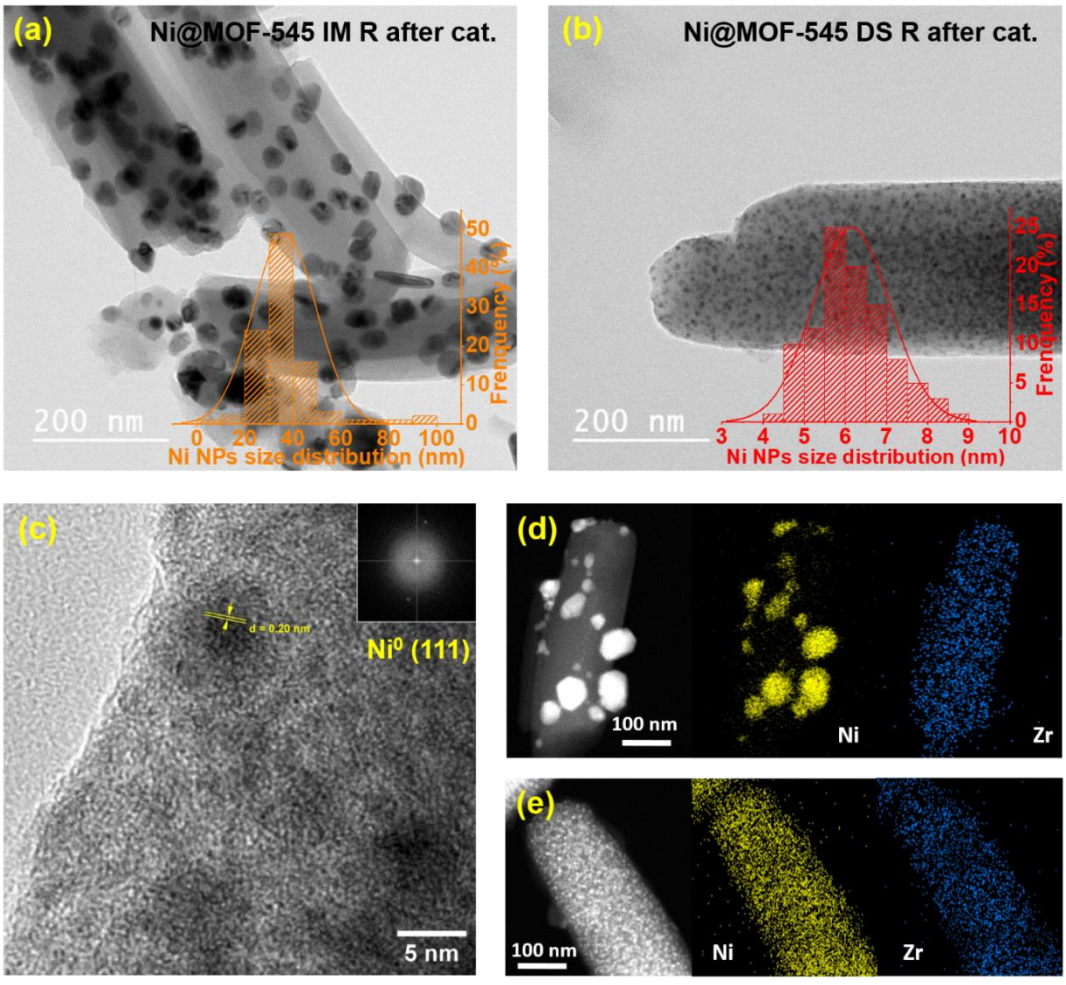

Figure 5. TEM images after catalysis of (a) **Ni@MOF-545 IM R** and (b) **Ni@MOF-545 DS R** (insert: size distribution of Ni NPs in the TEM images). (c) HR-TEM image after catalysis of **Ni@MOF-545 DS R** (insert: FFT of Ni NPs). HAADF-STEM image and EDX mapping after catalysis of (d) used **Ni@MOF-545 IM R** and (e) **Ni@MOF-545 DS R**. Samples were used in static conditions CO_2 methanation: CO_2/H_2 ratio 1:3, 10 bar, 300˚C, 3h.

Combining all these characterizations, the MOF-based support of our catalysts may be portrayed as follows. After the Ni loading and reduction steps, **Ni@MOF-545 DS R** is typically an amorphous and non-porous solid. Still, the XPS spectral analysis indicates that although the crystalline framework is collapsed, the integrity of constitutive sub-units of the MOF may be partially maintained, such as the porphyrinic linkers or the Zr-oxoclusters. The DRIFT analysis of **Ni@MOF-545 DS R** in the 1300-1700 cm^{-1} spectral region also shows that the typical features of the TCPP linkers are maintained (**Figure S16**). In addition, the far-IR DRIFT spectra of **Ni@MOF-545 DS R**, when compared to that of a tetragonal ZrO_2 thin film, exhibit unambiguous features associated with Zr-O bonds, allowing considering that Zr-oxoclusters are indeed present in the catalyst (**Figure S19a**). The restructuring of Zr-oxoclusters in MOFs upon thermal treatment has been described experimentally in details by Plateros-Plats et al. for another MOF, NU-1000, which shares the same architecture and Zr-nodes with MOF-545.[43] Finally, although the formation of amorphous carbon in our catalysts may not be excluded, the far-IR spectrum of **Ni@MOF-545 DS R** is significantly different from that collected from carbon black, for which no IR bands are observed but rather a strong and continuous absorption in the 100-500 cm^{-1} region (**Figure S19b**).

The above characterization results also allowed us to rationalise the enhanced catalytic activity of **Ni@MOF-545 DS R** for CO_2 methanation when compared to that of **Ni@MOF-545 IM R**. Two distinct factors seem to be at play in the enhancement of catalytic activity of the DS solid when compared to the IM one. First, the DS method used for loading Ni in MOF-545 has a beneficial impact on the subsequent dispersion of Ni NPs, whereby NPs form in a very homogeneously dispersed fashion within the solid, as opposed to the surface distribution of Ni NPs observed for the IM-prepared catalyst. Secondly, the DS method seems to avoid the sintering of Ni NPs upon reduction as it allows to form much smaller Ni NPs (< 8 nm) than the IM method (~40 nm), a distinctive feature that is maintained after catalysis. Notably, the catalytic activity of **Ni@MOF-545 DS R** for CO_2 methanation emanates exclusively from the portion of Ni NPs exposed at the surface of the MOF's rods, as indicated by the absence of porosity from BET measurements. As for **Ni@MOF-545 IM R**, the Ni NPs are deposited exclusively at the surface of the MOF support as evidenced by TEM. The higher catalytic activity of **Ni@MOF-545 DS R** when compared to that of **Ni@MOF-545 IM R** thus highlights the remarkable impact of the small size of the Ni NPs in the DS-prepared material, this knowing that **Ni@MOF-545 DS R** has a much lower amount of Ni exposed at the surface than **Ni@MOF-545 IM R**.

Interestingly, the structure sensitivity of metallic Ni NPs for CO_2 methanation has previously been explored in depth both experimentally and computationally.[28,53,54] Investigating metallic Ni NPs in the 1 to 10 nm size range, the authors have demonstrated that the most effective planes for CO_2 methanation were the (110) ones, while the (111) and (100) terraces barely showed any catalytic activity.[53] In the present work, **Ni@MOF-545 DS R** contains metallic Ni NPs in the 5-6 nm range, whereby the proportion of (110) facets associated with Ni NPs of this size[53] might contribute to its high catalytic activity for CO_2 methanation when compared to that of **Ni@MOF-545 IM R** possessing Ni NPs of much larger size (~40 nm). Our results thus tend to suggest that the Zr-based MOF-545 support might allow a high dispersion of small Ni^0 NPs due to its adapted porosity when using the double solvent method,[45] which allows a cooperation between the hydrophilic nickel species and Zr_6-oxoclusters, the latter being shown to participate also to the catalytic event, in line with earlier reports.[23,29]

CONCLUSIONS

We have prepared Ni@MOF composites using the Zr-based porphyrinic MOF-545 as a support for catalytic Ni^0 NPs using free-base or Cu-metalated porphyrin linkers. First, *in-situ* DRIFT spectroscopy

together with DFT calculations indicate that the Ni-free MOF-545 may be transformed into a catalytically active material in CO_2 hydrogenation conditions, producing CO and CH_4. We also ruled out any essential role of Cu in the observed methanation catalytic activity. Second, with the goal of synthesizing Ni@MOF catalysts for CO_2 methanation, we prepared Ni^0 NPs loaded MOF-545 composites, exploring two synthetic methods, i.e. the impregnation (IM) and double solvent (DS) methods, providing **Ni@MOF-545 IM R** and **Ni@MOF-545 DS R** catalysts upon H_2 reduction treatment. Both static and flow reactor conditions revealed the remarkable performances of **Ni@MOF-545 DS R** when compared to those of **Ni@MOF-545 IM R**, highlighting the critical impact of the Ni NPs preparation method on the resulting catalytic properties. We report 100% CH_4 selectivity, a high rate (595 $mmol_{CH4}$ g_{Ni}^{-1} h^{-1}) for the **Ni@MOF-545 DS R** catalyst. TEM images revealed a striking difference in the spatial dispersion and sizes of the Ni^0 NPs between DS- and IM-prepared samples. It was shown that the Ni^0 NPs are distributed exclusively over the surface of the solid in **Ni@MOF-545 IM R**, with a Ni^0 NPs size around 20-40 nm, while in **Ni@MOF-545 DS R**, much smaller Ni NPs with diameters of around 5 nm are homogeneously distributed both within the bulk and at the MOF surface. We infer that the built-in high density of hydrophilic Zr_6-oxoclusters in MOF-545 offers unique anchoring sites for stabilizing nickel species, a property optimized when using the DS method. The latter further allows inhibiting detrimental sintering of Ni NPs. We believe that this fundamental work will be applicable to the many unexplored Zr-based MOFs as active support to develop new and highly efficient CO_2 methanation catalysts.

EXPERIMENTAL SECTION

Materials

Meso-tetrakis(4-carboxyphenyl)porphyrin (H_2TCPP) was purchased from TCI Europe. Cu-TCPP was synthesized as described by Feng et al.[55] Zirconyl chloride octahydrate ($ZrOCl_2$•$8H_2O$) and Nickel(II) nitrate hexahydrate ($Ni(NO_3)_2$•$6H_2O$) were purchased from Alfa Aesar. 1,2-dichloroacetic acid was purchased from Sigma-Aldrich. *N,N*-dimethylformamide (DMF), acetone, methanol, and *n*-pentane were from Fisher Scientific. All chemicals were used as received.

Catalysts Synthesis

MOF-545 synthesis. MOF-545 was synthesized using reported protocols.[34,56] 65 mg of H_2TCPP, 325 mg of $ZrOCl_2.8H_2O$ and 2.5 mL of 1,2-dichloroacetic acid were mixed in 80 mL of DMF. The mixture was heated at 130 °C overnight. After cooling down to room temperature, the MOF was collected by centrifugation, and then washed twice with DMF and twice–with acetone. The MOF was further washed in a 25 mL DMF/2.5 mL 1M HCl mixture with agitation and heating at 130 °C for two hours. After cooling down to room temperature and then centrifugation, the obtained MOF was rinsed twice with DMF and twice with acetone. The MOF was further dispersed in 50 mL of acetone overnight. The final MOF product was collected by centrifugation and rinsing twice with acetone. The MOF was then dried at room temperature and activated at 120 °C under vacuum overnight for further use, collected as a purple powder (m = 67 mg). Characterization of the sample via PXRD and BET attested of the successful synthesis of MOF-545.

MOF-545(Cu) synthesis. MOF-545(Cu) was synthesized using a reported protocol.[57] 60 mg of Cu-TCPP, 370 mg of $ZrOCl_2.8H_2O$ and 2 mL of 1,2-dichloroacetic acid were mixed in 80 mL of DMF. The mixture was heated at 130 °C overnight. After cooling down to room temperature, the MOF was collected by centrifugation, and then washed twice with DMF and twice with acetone. The MOF was further washed in a 20 mL DMF/2 mL 1M HCl mixture with agitation and heating at 130 °C for two hours. After cooling down to room temperature and then centrifugation, the obtained MOF was rinsed

twice with DMF and twice with acetone, centrifuged, further dispersed in 50 mL of acetone overnight, collected by centrifugation and rinsed twice with acetone. The MOF was then dried at room temperature, collected as a powder and finally activated at 120 °C under vacuum overnight for further use (m = 65 mg). Inductively coupled plasma-mass spectroscopy (ICP-MS) analysis was performed, showing a Zr:Cu ratio of 3.04 (expected: 3.00), pointing towards the full metalation of the porphyrins.

Ni loading of MOF-545 and MOF-545(Cu) by impregnation method (IM): synthesis of Ni@MOF-545 IM and Ni@MOF-545(Cu) IM. The impregnation method was inspired by protocols previously reported for the synthesis of NP@MOF systems.[58] 100 mg of MOF-545 or MOF-545(Cu) were dispersed in 16 mL of methanol by sonication. 162 mg of $Ni(NO_3)_2$•$6H_2O$ (0.56 mmol) were then added into the suspension and stirred for 1 h. The solvent was evaporated under vacuum and the **Ni@MOF-545 IM** or **Ni@MOF-545(Cu) IM** solids dried at 100 °C.

Ni loading of MOF-545 by the double-solvent (DS) method: synthesis of Ni@MOF-545 DS. 100 mg of synthesized MOF-545 were dispersed in 20 mL of *n*-pentane by sonication. 800 µL of 0.5 M $Ni(NO_3)_2$•$6H_2O$ aqueous solution were then slowly added to the MOF suspension at a rate of 40 µL/min. The suspension was stirred for 3 h, and then the solvent removed by rotary evaporation. The obtained Ni-loaded MOF-545 product **Ni@MOF-545 DS** was further dried at 150 °C under vacuum overnight.

Ni@MOF-545 DS R. 50 mg of **Ni@MOF-545 DS** were reduced in a 5% H_2/Ar flow at 350 °C for 24 h. The reduced forms of **MOF-545**, **MOF-545(Cu)**, **Ni@MOF-545 IM** and **Ni@MOF-545(Cu) IM** were prepared using the same protocol, affording **MOF-545 R**, **MOF-545(Cu) R**, **Ni@MOF-545 IM R** and **Ni@MOF-545(Cu) IM R**, respectively.

Catalysts Characterizations

The crystallinity of the samples was analysed by powder X-ray diffraction using Cu Kα radiation ($\lambda_{K\alpha1}$ = 1.54056 Å, $\lambda_{K\alpha2}$ = 1.54439 Å) equipped with a Lynxeye detector (Bruker D8 Advance diffractometer) in Bragg–Brentano geometry. Thermogravimetric analyses (TGA) were performed on a Mettler Toledo TGA/DSC 1, STARe System ranging from room temperature to 700 °C (3 °C min^{-1}) under a 50 ml min^{-1} air flow. Scanning electron microscopy (SEM) images were captured using a ZEISS Ultra-55 scanning electron microscope. Transmission electron microscopy (TEM) was carried out using a JEOL 2100 Plus UHR microscope operating at 200 kV. The powdered samples were dispersed in ethanol, and then a drop was evaporated on a carbon-coated copper grid or a carbon-coated nickel grid. Scanning transmission electron microscopy (STEM) images using a high-angle annular dark-field (HAADF) detector were also acquired. The image contrast in this mode is strongly correlated to the atomic number: heavier elements contribute to brighter contrast (Z-contrast). Analytic investigations were performed with an energy dispersive X-ray (EDX, Oxford Instruments X-Max 80 SDD) spectrometer attached to the microscope column. The accurate Cu and Ni loading amounts in the MOFs samples were analyzed by ICP-coupled Atomic Emission Spectrometry (ICP-AES) (Thermo Scientific, iCAP™ PRO Duo ICP-OES). The MOF powders were digested by sonication in a mixture of H_2SO_4 (95 wt.%) and HNO_3 (65 wt.%) with a volume ratio of 1: 1.

Operando diffuse reflectance infrared Fourier transform (DRIFT) spectroscopy was carried out at the AILES Beamline of SOLEIL Synchrotron Light Facility (Saint Aubin, Paris, France) (Ref-AILES). The IR spectra were acquired using a Bruker IFS 125 MR spectrometer. Spectra were recorded in the mid infrared region (600 cm^{-1} to 4000 cm^{-1}) by using a KBr beam splitter, SiC internal source and a home-made 4.2K MCT detector (Ref-MCT). Each single spectrum was obtained by averaging 400 scans with a resolution of 4 cm^{-1}. The experiment was carried out by using a

commercial DRIFT cell (Harrick), allowing to record diffuse reflectance spectra under various catalytic conditions of temperature. The pressure and the flow of gas is controlled by a back-pressure regulator and three mass flow controllers, respectively (Bronkhorst). Prior to each experiment background spectra were acquired (KBr powder under vacuum). Absorption spectra were determined by the $A=-\log(I_s/I_0)$ relation, where I_s and I_0 are the light intensities of the sample and the background, respectively. For the CO_2 hydrogenation reactions, a known quantity of samples (15 mg) was activated for 12 h at 120 ˚C (10 ˚C /min) and under vacuum (10^{-4} mbar). Then, the sample was cooled down to room temperature. The activated sample is then exposed to a controlled flow of a mixture of CO_2/H_2 (3/9 mL/min) until reaching a pressure of 10 bars inside the reactor. In a second step, the sample was heated up from RT to 120 ˚C with a ramp of 5 ˚C /min and kept at 120 ˚C to collect DRIFT spectra. Then, the sample chamber was further heated up to 200 ˚C (ramp of 5 ˚C /min) and kept at 200 ˚C to collect DRIFT spectra. Later, the sample chamber was heated up from 200 ˚C to 300 ˚C (ramp of 20 ˚C /min) and kept at 300 ˚C to collect DRIFT spectra.

Catalyst powder was stored under inert atmosphere prior XPS analysis. Few milligrams of material were then deposited on conductive copper tape. Using this procedure, the samples have been exposed to air less than 2 minutes. Regular XPS analyses were conducted on a Thermofisher Scientific Nexsa equipped with a monochromated Al-Kα anode (1486.6 eV) and a dual flood gun (low energy electron and ion). High energy resolution spectral windows of interest were recorded with a 400 µm spot size. The photoelectron detection was performed perpendicularly to the surface using a constant analyzer energy (CAE) mode (20 eV pass energy) and a 0.1 eV energy step. Quantification was performed based on the O 1s, C 1s, N 1s, Ni 2p and Zr 3d photopeak areas after a Shirley type background subtraction using the Thermofisher Scientific Avantage© software and its "ALTHERMO1" library as sensitivity factor collection.

In addition, DFT calculations were carried out to characterize the behaviour of the Zr_6 nodes of MOF-545 upon heating treatment. Full details are given in SI.

CO_2 hydrogenation experiment

Static conditions: CO_2 hydrogenation tests were carried out in a stainless-steel high-pressure reactor (Parr, 4790 model, 25 mL) equipped with an electric oven and temperature controller (Equilabo). As a typical run, a catalyst pellet (15 mg) was fed into the autoclave. The catalyst pellet was slightly hand pressed using a die set (diameter of 8 mm). After replacing air in the reactor with a CO_2/H_2 (1:3, molar ratio) gas mixture for 4 times, the reactor was pressurized to 10 bar at ambient temperature. Then, the Parr reactor was heated up to 300 ˚C and kept at this temperature for 3 h. After the reactor was cool down to room temperature, and depressurized to 1 bar (ambient pressure), all the gases were collected in a gas sampling bag (1 L tedlar® plv gas sampling bag w/thermogreen® lb-2 septa). The composition of gas in the gas sampling bag was analyzed with a gas chromatograph (GC, SRI Instruments, MG#5 GC, Ar carrier). Quantification of carbon-based products was carried out by a flame-ionization detector. CH_4 and CO were separated using a 3 m molecular sieve column. A control experiment using the empty reactor without any MOF or catalyst was carried out under the same CO_2 hydrogenation conditions. The GC analysis showed that no product was detected in the control experiment. The CH_4 and CO selectivities (CH_4 and CO were the only carbon products of CO_2 hydrogenation detected here) were defined as follows:

$$S_{CH4}(\%) = \frac{R_{(CH4)}}{R_{(CH4)} + R_{(CO)}} \times 100$$

$$S_{CO}(\%) = \frac{R_{(CO)}}{R_{(CH4)} + R_{(CO)}} \times 100$$

where $R_{(CH4)}$ is the CH_4 production rate, and $R_{(CO)}$ is the CO production rate.

Flow reactor conditions: CO_2 hydrogenation tests were conducted in a fixed-bed continuous flow reactor at 300 ˚C and 10 bar over 15 mg catalyst powders. The reactor was heated by an electric oven equipped with a temperature controller. All gases were monitored by calibrated mass flow controllers. The $CO_2/H_2/N_2$ gas mixture with the flow rate of 3/9/10 mL min^{-1} was used for CO_2 methanation. The gas phase products were followed by in situ infrared spectroscopy, and the real-time online GC (INFICON Micro GC Fusion) quantified the production of products. The CO_2 conversion of the best-performed **Ni@MOF-545 DS R** sample (100% selectivity of CH_4) was calculated as follows:

$$X_{CO2}(\%) = \frac{C_{in(CO2)} - C_{out(CO2)}}{C_{in(CO2)}} \times 100 = \frac{C_{out(CH4)}}{C_{in(CO2)}} \times 100$$

where $C_{in(CO2)}$ is the inlet CO_2 concentration, $C_{out(CO2)}$ is the outlet CO_2 concentration, and $C_{(CH4)}$ is the outlet CH_4 concentration.

SUPPORTING INFORMATION

Experimental details, including PXRD, TGA, DRIFT spectra, XPS, TEM, HAADF-STEM, EDX, ICP-AES analysis and computational details. This material is available free of charge via the Internet at http://pubs.acs.org.

AUTHOR INFORMATION

*E-mail: caroline.mellot-draznieks@college-de-france.fr (C.-M.-D.)
*E-mail: jean-blaise.brubach@synchrotron-soleil.fr (J.-B.B.)

Notes

There are no conflicts to declare.

ACKNOWLEDGMENTS

This work was supported by a grant of the Agence Nationale de la Recherche (ANR-21-CE07-0028 and ANR-21-CE50-0024). A. S.-D. acknowledges the Spanish Ministry of Universities and the European Union - Next Generation EU for their financial support through a Margarita Salas grant. F. P.-H., A.S.-D. and C. M.-D. thank GENCI (CINES/TGCC) for HPC resources through the 2022-2023 grant A0130907343. We thank Georges Mouchaham at IMAP for allowing additional BET measurements. C.M.-D. is grateful for financial support from the Paris Ile-de- France Region – DIM "Respore."

REFERENCES

(1) Gholampour, N.; Zhao, Y.; Devred, F.; Sassoye, C.; Casale, S.; Debecker, D. P. CO_2 Methanation over Cobalt Nanoparticles Embedded in ZIF-L–Derived Porous Carbon. *ChemCatChem* **2023**, *15* (5), 1–9. https://doi.org/10.1002/cctc.202201338.

(2) Ocampo, F.; Louis, B.; Kiwi-Minsker, L.; Roger, A. C. Effect of Ce/Zr Composition and Noble Metal Promotion on Nickel Based $Ce_xZr_{1-X}O_2$ Catalysts for Carbon Dioxide Methanation. *Appl. Catal. A Gen.* **2011**, *392* (1–2), 36–44. https://doi.org/10.1016/j.apcata.2010.10.025.

(3) Álvarez, A.; Bansode, A.; Urakawa, A.; Bavykina, A. V.; Wezendonk, T. A.; Makkee, M.; Gascon, J.; Kapteijn, F. Challenges in the Greener Production of Formates/Formic Acid, Methanol, and DME by Heterogeneously Catalyzed CO_2 Hydrogenation Processes. *Chem. Rev.* **2017**, *117* (14), 9804–9838. https://doi.org/10.1021/ACS.CHEMREV.6B00816.

(4) An, B.; Zeng, L.; Jia, M.; Li, Z.; Lin, Z.; Song, Y.; Zhou, Y.; Cheng, J.; Wang, C.; Lin, W. Molecular Iridium Complexes in Metal−Organic Frameworks Catalyze CO_2 Hydrogenation via Concerted Proton and Hydride Transfer. *J. Am. Chem. Soc* **2017**, *139*, 17747-17750. https://doi.org/10.1021/jacs.7b10922.

(5) Larmier, K.; Liao, W.-C.; Tada, S.; Lam, E.; Verel, R.; Bansode, A.; Urakawa, A.; Comas-Vives, A.; Copéret, C. CO_2-to-Methanol Hydrogenation on Zirconia-Supported Copper Nanoparticles: Reaction Intermediates and the Role of the Metal-Support Interface . *Angew. Chemie* **2017**, *129* (9), 2358–2363. https://doi.org/10.1002/ange.201610166.

(6) Xu, D.; Wang, Y.; Ding, M.; Hong, X.; Liu, G.; Tsang, S. C. E. Advances in Higher Alcohol Synthesis from CO_2 Hydrogenation. *Chem* **2021**, *7* (4), 849–881. https://doi.org/10.1016/j.chempr.2020.10.019.

(7) Wang, L.; Wang, I.; Zhang, J.; Liu, X.; Wang, H.; Zhang, E.; Yang, Q.; Ma, J.; Dong, X.; Eung, S.; Yoo, J.; Kim, J.-G.; Meng, X.; Xiao, S. Selective Hydrogenation of CO_2 to Ethanol over Cobalt Catalysts. *Angew. Chemie* **2018**, *57* (21), 6104–6108. https://doi.org/10.1002/ange.201800729.

(8) Bai, S.; Shao, Q.; Wang, P.; Dai, Q.; Wang, X.; Huang, X. Highly Active and Selective Hydrogenation of CO_2 to Ethanol by Ordered Pd-Cu Nanoparticles. *J. Am. Chem. Soc.* **2017**, *139* (20), 6827–6830. https://doi.org/10.1021/jacs.7b03101.

(9) Shen, L.; Xu, J.; Zhu, M.; Han, Y. F. Essential Role of the Support for Nickel-Based CO_2 Methanation Catalysts. *ACS Catal.* **2020**, *10* (24), 14581–14591. https://doi.org/10.1021/acscatal.0c03471.

(10) Li, W.; Wang, H.; Jiang, X.; Zhu, J.; Liu, Z.; Guo, X.; Song, C. A Short Review of Recent Advances in CO_2 Hydrogenation to Hydrocarbons over Heterogeneous Catalysts. *RSC Adv.* **2018**, *8*, 7651–7669. https://doi.org/10.1039/c7ra13546g.

(11) Len, T.; Luque, R. Addressing the CO_2 Challenge through Thermocatalytic Hydrogenation to Carbon Monoxide, Methanol and Methane. *Green Chem.* **2023**, *25* (2), 490–521. https://doi.org/10.1039/d2gc02900f.

(12) Garbarino, G.; Wang, C.; Cavattoni, T.; Finocchio, E.; Riani, P.; Flytzani-Stephanopoulos, M.; Busca, G. A Study of Ni/La-Al_2O_3 Catalysts: A Competitive System for CO_2 Methanation. *Appl. Catal. B Environ.* **2019**, *248*, 286–297. https://doi.org/10.1016/j.apcatb.2018.12.063.

(13) Ye, R. P.; Liao, L.; Reina, T. R.; Liu, J.; Chevella, D.; Jin, Y.; Fan, M.; Liu, J. Engineering Ni/SiO_2 Catalysts for Enhanced CO_2 Methanation. *Fuel* **2021**, *285* (2020). https://doi.org/10.1016/j.fuel.2020.119151.

(14) Lv, C.; Xu, L.; Chen, M.; Cui, Y.; Wen, X.; Li, Y.; Wu, C. E.; Yang, B.; Miao, Z.; Hu, X.; Shou, Q. Recent Progresses in Constructing the Highly Efficient Ni Based Catalysts With Advanced Low-Temperature Activity Toward CO_2 Methanation. *Front. Chem.* **2020**, *8*, 1–32. https://doi.org/10.3389/fchem.2020.00269.

(15) Ding, M.; Flaig, R. W.; Jiang, H. L.; Yaghi, O. M. Carbon Capture and Conversion Using Metal–Organic Frameworks and MOF-Based Materials. *Chem. Soc. Rev.* **2019**, *48* (10), 2783–2828. https://doi.org/10.1039/C8CS00829A.

(16) Zhang, Q.; Wang, S.; Dong, M.; Fan, W. CO_2 Hydrogenation on Metal-Organic Frameworks-Based Catalysts: A Mini Review. *Front. Chem.* **2022**, *10*, 1–7. https://doi.org/10.3389/fchem.2022.956223.

(17) Gulati, S.; Vijayan, S.; Mansi; Kumar, S.; Harikumar, B.; Trivedi, M.; Varma, R. S. Recent Advances in the Application of Metal-Organic Frameworks (MOFs)-Based Nanocatalysts for Direct Conversion of Carbon Dioxide (CO2) to Value-Added Chemicals. *Coord. Chem. Rev.* **2023**, *474*, 214853. https://doi.org/10.1016/j.ccr.2022.214853.

(18) Lu, X.; Song, C.; Qi, X.; Li, D.; Lin, L. Confinement Effects in Well-Defined Metal–Organic Frameworks (MOFs) for Selective CO_2 Hydrogenation: A Review. *Int. J. Mol. Sci.* **2023**, *24* (4), 4228. https://doi.org/10.3390/ijms24044228.

(19) Gutterød, E. S.; Lazzarini, A.; Fjermestad, T.; Kaur, G.; Manzoli, M.; Bordiga, S.; Svelle, S.; Lillerud, K. P.; Skúlason, E.; Øien-ØDegaard, S.; Nova, A.; Olsbye, U. Hydrogenation of CO_2 to Methanol by Pt Nanoparticles Encapsulated in UiO-67: Deciphering the Role of the Metal-Organic Framework. *J. Am. Chem. Soc.* **2020**, *142* (2), 999–1009. https://doi.org/10.1021/jacs.9b10873.

(20) An, B.; Zhang, J.; Cheng, K.; Ji, P.; Wang, C.; Lin, W. Confinement of Ultrasmall Cu/ZnO_x Nanoparticles in Metal-Organic Frameworks for Selective Methanol Synthesis from Catalytic Hydrogenation of CO_2. *J. Am. Chem. Soc.* **2017**, *139* (10), 3834–3840. https://doi.org/10.1021/jacs.7b00058.

(21) Zhen, W.; Li, B.; Lu, G.; Ma, J. Enhancing Catalytic Activity and Stability for CO_2 Methanation on Ni@MOF-5 via Control of Active Species Dispersion. *Chem. Commun.* **2015**, *51* (9), 1728–1731. https://doi.org/10.1039/c4cc08733j.

(22) Mihet, M.; Grad, O.; Blanita, G.; Radu, T.; Lazar, M. D. Effective Encapsulation of Ni Nanoparticles in Metal-Organic Frameworks and Their Application for CO_2 Methanation. *Int. J. Hydrogen Energy* **2019**, *44* (26), 13383–13396. https://doi.org/10.1016/j.ijhydene.2019.03.259.

(23) Zhen, W.; Gao, F.; Tian, B.; Ding, P.; Deng, Y.; Li, Z.; Gao, H.; Lu, G. Enhancing Activity for Carbon Dioxide Methanation by Encapsulating (111) Facet Ni Particle in Metal–Organic Frameworks at Low Temperature. *J. Catal.* **2017**, *348*, 200–211. https://doi.org/10.1016/j.jcat.2017.02.031.

(24) Zhao, Z. W.; Zhou, X.; Liu, Y. N.; Shen, C. C.; Yuan, C. Z.; Jiang, Y. F.; Zhao, S. J.; Ma, L. B.; Cheang, T. Y.; Xu, A. W. Ultrasmall Ni Nanoparticles Embedded in Zr-Based MOFs Provide High Selectivity for CO_2 Hydrogenation to Methane at Low Temperatures. *Catal. Sci. Technol.* **2018**, *8* (12), 3160–3165. https://doi.org/10.1039/c8cy00468d.

(25) Lin, X.; Wang, S.; Tu, W.; Hu, Z.; Ding, Z.; Hou, Y.; Xu, R.; Dai, W. MOF-Derived Hierarchical Hollow Spheres Composed of Carbon-Confined Ni Nanoparticles for Efficient CO_2 Methanation. *Catal. Sci. Technol.* **2019**, *9* (3), 731–738. https://doi.org/10.1039/c8cy02329h.

(26) Li, Y. T.; Zhou, L.; Cui, W. G.; Li, Z. F.; Li, W.; Hu, T. L. Iron Promoted MOF-Derived Carbon Encapsulated NiFe Alloy Nanoparticles Core-Shell Catalyst for CO_2 methanation. *J. CO2 Util.* **2022**, *62*, 102093. https://doi.org/10.1016/j.jcou.2022.102093.

(27) Zurrer, T.; Wong, K.; Horlyck, J.; Lovell, E. C.; Wright, J.; Bedford, N. M.; Han, Z.; Liang, K.; Scott, J.; Amal, R. Mixed-Metal MOF-74 Templated Catalysts for Efficient Carbon Dioxide Capture and Methanation. *Adv. Funct. Mater.* **2021**, *31* (9), 1–12. https://doi.org/10.1002/adfm.202007624.

(28) Vogt, C.; Groeneveld, E.; Kamsma, G.; Nachtegaal, M.; Lu, L.; Kiely, C. J.; Berben, P. H.; Meirer, F.; Weckhuysen, B. M. Unravelling Structure Sensitivity in CO2 Hydrogenation over Nickel. *Nat. Catal.* **2018**, *1* (2), 127–134. https://doi.org/10.1038/s41929-017-0016-y.

(29) Jia, X.; Zhang, X.; Rui, N.; Hu, X.; Liu, C. jun. Structural Effect of Ni/ZrO_2 Catalyst on CO_2 Methanation with Enhanced Activity. *Appl. Catal. B Environ.* **2019**, *244*, 159–169. https://doi.org/10.1016/j.apcatb.2018.11.024.

(30) Zeng, L.; Wang, Y.; Li, Z.; Song, Y.; Zhang, J.; Wang, J.; He, X.; Wang, C.; Lin, W. Highly Dispersed Ni Catalyst on Metal-Organic Framework-Derived Porous Hydrous Zirconia for CO_2 Methanation. *ACS Appl. Mater. Interfaces* **2020**, *12* (15), 17436–17442. https://doi.org/10.1021/acsami.9b23277.

(31) Qi, S. C.; Yang, Z. H.; Zhu, R. R.; Lu, X. J.; Xue, D. M.; Liu, X. Q.; Sun, L. B. The Cascade Catalysis of the Porphyrinic Zirconium Metal-Organic Framework PCN-224-Cu for CO_2 conversion to Alcohols. *J. Mater. Chem. A* **2021**, *9* (43), 24510–24516. https://doi.org/10.1039/d1ta06950k.

(32) Rungtaweevoranit, B.; Baek, J.; Araujo, J. R.; Archanjo, B. S.; Choi, K. M.; Yaghi, O. M.; Somorjai, G. A. Copper Nanocrystals Encapsulated in Zr-Based Metal-Organic Frameworks for Highly Selective CO_2 Hydrogenation to Methanol. *Nano Lett.* **2016**, *16* (12), 7645–7649. https://doi.org/10.1021/ACS.NANOLETT.6B03637/SUPPL_FILE/NL6B03637_SI_001.PDF.

(33) Stawowy, M.; Ciesielski, R.; Maniecki, T.; Matus, K.; Łużny, R.; Trawczynski, J.; Silvestre-Albero, J.; Łamacz, A. CO_2 Hydrogenation to Methanol over Ce and Zr Containing UiO-66 and Cu/UiO-66. *Catalysts* **2019**, *10* (1), 39. https://doi.org/10.3390/CATAL10010039.

(34) Paille, G.; Gomez-Mingot, M.; Roch-Marchal, C.; Lassalle-Kaiser, B.; Mialane, P.; Fontecave, M.; Mellot-Draznieks, C.; Dolbecq, A. A Fully Noble Metal-Free Photosystem Based on Cobalt-Polyoxometalates Immobilized in a Porphyrinic Metal-Organic Framework for Water Oxidation. *J. Am. Chem. Soc.* **2018**, *140* (10), 3613–3618. https://doi.org/10.1021/jacs.7b11788.

(35) Zhang, J.; An, B.; Li, Z.; Cao, Y.; Dai, Y.; Wang, W.; Zeng, L.; Lin, W.; Wang, C. Neighboring Zn−Zr Sites in a Metal−Organic Framework for CO_2 Hydrogenation. *J. Am. Chem. Soc* **2021**, *143* (23), 8829–8837. https://doi.org/10.1021/jacs.1c03283.

(36) Hadjiivanov, K. I.; Panayotov, D. A.; Mihaylov, M. Y.; Ivanova, E. Z.; Chakarova, K. K.; Andonova, S. M.; Drenchev, N. L. Power of Infrared and Raman Spectroscopies to Characterize Metal-Organic Frameworks and Investigate Their Interaction with Guest Molecules. *Chem. Rev.* **2021**, *121* (3), 1286–1424. https://doi.org/10.1021/acs.chemrev.0c00487.

(37) Grissom, T. G.; Sharp, C. H.; Usov, P. M.; Troya, D.; Morris, A. J.; Morris, J. R. Benzene, Toluene, and Xylene Transport through UiO-66: Diffusion Rates, Energetics, and the Role of Hydrogen Bonding. *J. Phys. Chem. C* **2018**, *122* (28), 16060–16069. https://doi.org/10.1021/acs.jpcc.8b03356.

(38) Shearer, G. C.; Forselv, S.; Chavan, S.; Bordiga, S.; Mathisen, K.; Bjørgen, M.; Svelle, S.; Lillerud, K. P. In Situ Infrared Spectroscopic and Gravimetric Characterisation of the Solvent Removal and Dehydroxylation of the Metal Organic Frameworks UiO-66 and UiO-67. *Top. Catal.* **2013**, *56* (9–10), 770–782. https://doi.org/10.1007/s11244-013-0027-0.

(39) Hadjiivanov, K. I.; Panayotov, D. A.; Mihaylov, M. Y.; Ivanova, E. Z.; Chakarova, K. K.; Andonova, S. M.; Drenchev, N. L. Power of Infrared and Raman Spectroscopies to Characterize Metal-Organic Frameworks and Investigate Their Interaction with Guest Molecules. *Chem. Rev*. **2021**, *121*, 1286–1424. https://doi.org/10.1021/acs.chemrev.0c00487.

(40) Wan, J.; Wang, H.; Wu, Z.; Shun, Y. C.; Zheng, X.; Phillips, D. L. Resonance Raman Spectroscopy and Density Functional Theory Calculation Study of Photodecay Dynamics of Tetra(4-Carboxyphenyl) Porphyrin. *Phys. Chem. Chem. Phys.* **2011**, *13* (21), 10183–10190. https://doi.org/10.1039/c0cp02933e.

(41) Ling, S.; Slater, B. Dynamic Acidity in Defective UiO-66. *Chem. Sci.* **2016**, *7* (7), 4706–4712. https://doi.org/10.1039/c5sc04953a.

(42) Vandichel, M.; Hajek, J.; Vermoortele, F.; Waroquier, M.; De Vos, D. E.; Van Speybroeck, V. Active Site Engineering in UiO-66 Type Metal-Organic Frameworks by Intentional Creation of Defects: A Theoretical Rationalization. *CrystEngComm* **2015**, *17* (2), 395–406.

https://doi.org/10.1039/c4ce01672f.

(43) Platero-Prats, A. E.; Mavrandonakis, A.; Gallington, L. C.; Liu, Y.; Hupp, J. T.; Farha, O. K.; Cramer, C. J.; Chapman, K. W. Structural Transitions of the Metal-Oxide Nodes within Metal-Organic Frameworks: On the Local Structures of NU-1000 and UiO-66. *J. Am. Chem. Soc.* **2016**, *138* (12), 4178–4185. https://doi.org/10.1021/jacs.6b00069.

(44) Yang, K.; Jiang, J. Computational Design of a Metal-Based Frustrated Lewis Pair on Defective UiO-66 for CO_2 hydrogenation to Methanol. *J. Mater. Chem. A* **2020**, *8* (43), 22802–22815. https://doi.org/10.1039/d0ta07051c.

(45) Aijaz, A.; Karkamkar, A.; Choi, Y. J.; Tsumori, N.; Rönnebro, E.; Autrey, T.; Shioyama, H.; Xu, Q. Immobilizing Highly Catalytically Active Pt Nanoparticles inside the Pores of Metal-Organic Framework: A Double Solvents Approach. *J. Am. Chem. Soc.* **2012**, *134* (34), 13926–13929. https://doi.org/10.1021/ja3043905.

(46) Biesinger, M. C.; Payne, B. P.; Lau, L. W. M.; Gerson, A.; Smart, R. S. C. X-Ray Photoelectron Spectroscopic Chemical State Quantification of Mixed Nickel Metal, Oxide and Hydroxide Systems. *Surf. Interface Anal.* **2009**, *41* (4), 324–332. https://doi.org/10.1002/sia.3026.

(47) Biesinger, M. C.; Payne, B. P.; Grosvenor, A. P.; Lau, L. W. M.; Gerson, A. R.; Smart, R. S. C. Resolving Surface Chemical States in XPS Analysis of First Row Transition Metals, Oxides and Hydroxides: Cr, Mn, Fe, Co and Ni. *Appl. Surf. Sci.* **2011**, *257* (7), 2717–2730. https://doi.org/10.1016/j.apsusc.2010.10.051.

(48) Moulder, J. F.; Stickle, W. F.; Sobol, P. E.; Bomben, K. D. *Handbook of X-ray Photoelectron Spectroscopy*; Chastain, J., Ed.; Perkin-Elmer Corporation, 1992.

(49) Manoli, J.-M.; Potvin,C.; Muhler,M.; Wild, U.; Resofszki, G.; Buchholz, T.; Paal, Z. Evolution of the Catalytic Activity in Pt/Sulfated Zirconia Catalysts: Structure, Composition, and Catalytic Properties of the Catalyst Precursor and the Calcined Catalyst. *J. Catal.* **1998**, 178, 338–351. https://doi.org/10.1006/jcat.1998.2104.

(50) Wang, H.; Li, Q.; Chen, J.; Chen J.; Jia, H. Efficient Solar-Driven CO_2 Methanation and Hydrogen Storage Over Nickel Catalyst Derived from Metal–Organic Frameworks with Rich Oxygen Vacancies. *Adv. Sci.* **2023**, *10*, 2304406. https://doi-org.inc.bib.cnrs.fr/10.1002/advs.202304406.

(51) Lin, J.; Ma, C.; Wang, Q.; Xu, Y.; Ma, G.; Wang, J.; Wang, H.; Dong, C.; Zhang, C.; Ding, M., Enhanced low-temperature performance of CO_2 methanation over mesoporous Ni/Al_2O_3-ZrO_2 catalysts. *Appl. Catal. B-Environ.* **2019**, *243*, 262. https://doi.org/10.1016/j.apcatb.2018.10.059.

(52) Sato, A. G.; Volanti, D. P.; Meira, D. M.; Damyanova, S.; Longo, E.; Bueno, J. M. C. Effect of the ZrO_2 phase on the structure and behavior of supported Cu catalysts for ethanol conversion. *J. Catal.* **2013**, *307*, 1-17. https://doi.org/10.1016/j.jcat.2013.06.022.

(53) Sterk, E. B.; Nieuwelink, A. E.; Monai, M.; Louwen, J. N.; Vogt, E. T. C.; Filot, I. A. W.; Weckhuysen, B. M. Structure Sensitivity of CO_2 Conversion over Nickel Metal Nanoparticles Explained by Micro-Kinetics Simulations. *JACS Au* **2022**, *2* (12), 2714–2730. https://doi.org/10.1021/jacsau.2c00430.

(54) Vogt, C.; Monai, M.; Sterk, E. B.; Palle, J.; Melcherts, A. E. M.; Zijlstra, B.; Groeneveld, E.; Berben, P. H.; Boereboom, J. M.; Hensen, E. J. M.; Meirer, F.; Filot, I. A. W.; Weckhuysen, B. M. Understanding Carbon Dioxide Activation and Carbon–Carbon Coupling over Nickel. *Nat. Commun.* **2019**, *10* (1), 1–10. https://doi.org/10.1038/s41467-019-12858-3.

(55) Feng, D.; Gu, Z. Y.; Li, J. R.; Jiang, H. L.; Wei, Z.; Zhou, H. C. Zirconium-Metalloporphyrin PCN-222: Mesoporous Metal-Organic Frameworks with Ultrahigh Stability as Biomimetic

Catalysts. *Angew. Chemie - Int. Ed.* **2012**, *51* (41), 10307–10310. https://doi.org/10.1002/anie.201204475.

(56) Kelty, M. L.; Morris, W.; Gallagher, A. T.; Anderson, J. S.; Brown, K. A.; Mirkin, C. A.; Harris, T. D. High-Throughput Synthesis and Characterization of Nanocrystalline Porphyrinic Zirconium Metal-Organic Frameworks. *Chem. Commun.* **2016**, *52* (50), 7854–7857. https://doi.org/10.1039/c6cc03264h.

(57) Benseghir, Y.; Solé-Daura, A.; Cairnie, D. R.; Robinson, A. L.; Duguet, M.; Mialane, P.; Gairola, P.; Gomez-Mingot, M.; Fontecave, M.; Iovan, D.; Bonnett, B.; Morris, A. J.; Dolbecq, A.; Mellot-Draznieks, C. Unveiling the Mechanism of the Photocatalytic Reduction of CO_2 to Formate Promoted by Porphyrinic Zr-Based Metal-Organic Frameworks. *J. Mater. Chem. A* **2022**, *10* (35), 18103–18115. https://doi.org/10.1039/d2ta04164b.

(58) Yu, Y.; Liu, C. X.; Fan, X. Y.; Wei, Y. J.; Lin, R. De; Yao, Y.; Shi, M. L.; Wang, N.; Yu, X. Q. A Cascade Catalytic System of Photocatalytic Oxidation Based on Cu@PCN-222(Ni) and Enzyme Catalysis for the Synthesis of Chalcone Compounds in One Pot. *J. Catal.* **2022**, *415*, 102–111. https://doi.org/10.1016/j.jcat.2022.10.008.

SYNOPSIS TOC